Proceedings of the ASME 2023
Pressure Vessels & Piping Conference
PVP2023
July 16-21, 2023, Atlanta, Georgia

PVP2023-106216

THE EFFECT OF LOSS OF CONSTRAINT ON THE INITIATION OF DUCTILE FRACTURE IN A MINI-CT

M. Li[1,2,*], R. Chaouadi[1], I. Uytdenhowen[1], T. Pardoen[2], G. Bonny[1]

[1] Belgian Nuclear Research Centre (SCK CEN), Institute of Nuclear Energy and Technology (NET); Boeretang 200, 2400 Mol, Belgium.
[2] Institute of Mechanics, Materials and Civil Engineering (IMMC), Université catholique de Louvain; B-1348 Louvain-la-Neuve, Belgium.
[*] Corresponding author, E-mail: meng.li@sckcen.be

ABSTRACT

As one of the most appealing miniaturized geometries for fracture toughness characterization, the miniature compact tension (mini-CT) geometry was demonstrated to provide reliable fracture toughness measurement in the ductile-to-brittle transition regime and Master Curve assessment. However, when using a mini-CT in the upper shelf (fully ductile) regime, the ductile crack initiation and the crack growth resistance tend to be underestimated for most of the investigated RPV steels.

Previous experimental investigations have attributed the underestimation of the crack resistance properties to two concurrent processes related to loss of constraint and cold working occurring in the ligament ahead of crack tip during cracking, and gave an engineering size correction that mainly accounts for the thickness of the specimens. In this study, finite element simulations and two micromechanics-based approaches: the Rice-Tracey void growth model and Thomason void coalescence model are combined, aimed at investigating the role that the loss of constraint plays in the initiation of ductile fracture in a mini-CT and providing numerical evidence to support the proposal of the size correction on the critical fracture toughness. The final objective of this paper is to estimate the ductile crack initiation behavior that would be obtained from a standard 1T-CT specimen by applying appropriate size correction on a mini-CT.

The results show that the method incorporating the finite element simulations and two micromechanics-based approaches can well describe the effects of loss of constraint for different materials, thus contributing to the size correction of critical fracture toughness of mini-CT in various conditions.

Keywords: mini-CT, loss of constraint, ductile fracture, finite element simulation, micromechanics-based approach, size correction

1. INTRODUCTION

In the context of the fracture toughness characterization of reactor pressure vessel (RPV) steel, mini-CT specimens (see Figure 1) have been widely tested to replace conventional large geometries to provide meaningful toughness values. In the ductile to brittle transition region, significant smaller fracture sampling area in front of the crack tip of a mini-CT leads to lower probability for triggering cleavage fracture, thus exhibiting higher toughness value [1]. The statistical nature of the fracture toughness brought by the mini-CT geometry can still be well represented with the help of the Master Curve approach [2]. The associated size correction method offers good compensation for the overestimated fracture toughness.

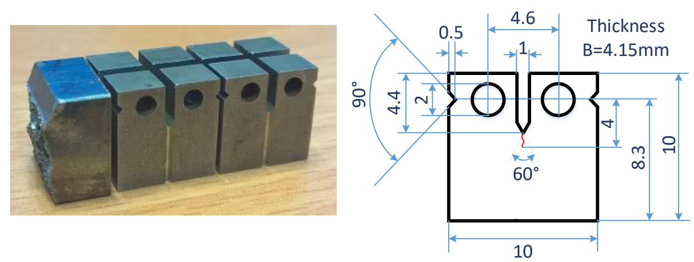

Figure 1: GEOMETRY OF MINI-CT SPECIMEN

In the upper shelf where fully ductile fracture behavior is considered, a lot of tests performed at Belgian Nuclear Research Centre (SCK CEN) show that the crack growth resistance curves (*J-R* curves) are often underestimated due to the effect of loss of constraint when using the mini-CT geometry. Subsequent critical fracture toughness (J_Q) of mini-CTs defined from the *J-R* curves also exhibits lower values. Even so, the mini-CT geometry is believed to provide effective resistance curves by applying appropriate size correction in a way similar to that in the transition region. Chaouadi et al. [3] proposed a simple engineering size correction based on the relative size of 1T-CT geometry and mini-CT geometry. The 1T-corrected *J-R* curve of the mini-CT geometry showed a reasonable agreement with the *J-R* curve determined from the 1T-CT geometry, suggesting the possibility of transferring *J-R* curves and even critical fracture toughness values from the mini-CT to the 1T-CT. However, previous research mainly lies in the size effect on the full *J-R* curve, typically the region between two construction lines. In this paper, another property that is potentially influenced by the reduction of specimen size, namely the initiation toughness of ductile fracture, is investigated. Finite element simulations as well as micromechanics-based approaches are combined to provide accurate assessment to the effect of loss of constraint on the critical fracture toughness that corresponds to the initiation of ductile fracture.

2. EXPERIMENTAL DATA ANALYSIS

The study on the initiation of ductile fracture requires a critical fracture parameter that can characterize the onset of fracture accurately. As an engineering approximation of ductile fracture initiation in ASTM E1820 [4], J_Q is generally defined as the intersection of the *J-R* curve and the 0.2 mm offset line, which is the J value corresponding to 0.2 mm crack extension beyond blunting. For the mini-CT geometry, the corresponding absolute crack extension of J_Q is around 0.5 mm (see Figure 2-a), which already reaches 50% of the maximum crack extension capacity of a mini-CT ($\Delta a_{max,mini\text{-}CT} = 0.25(W\text{-}a_0) \sim 1$ mm). It is a considerably large value compared to the ratio of $\Delta a_{JQ}/\Delta a_{max,1T\text{-}CT} = 15\%$ for a 1T-CT. Therefore, J_Q is no longer appropriate for characterizing the fracture toughness of mini-CT at the onset of ductile fracture, considering that at this point the mini-CT is already in the middle of a stable crack extension. In this paper, another critical value of J, $J_{0.2\,mm}$, is introduced as the critical toughness corresponding to the crack initiation. It was firstly considered by the standard ESIS P2-92 [5] and it provides better descriptions of the initiation of ductile fracture as it corresponds to 0.2 mm absolute crack extension (blunting included). As shown in Figure 2 (a), three mini-CT specimens were tested to three different load levels, the approximate positions of the three load levels are indicated on the *J-R* curve of mini-CT. From the microscope pictures shown in the same figure, crack extension is clearly observed from the fracture surfaces of the specimen 2 and 3. Evidence for crack initiation in specimen 1 can be found in Figure 2 (b). At the crack front region of specimen 1, fatigue pre-crack zone, stretch zone, ductile fracture extension zone and cleavage zone can be clearly identified. The significant crack tip blunting and ductile crack growth shown in region b and region c suggests that ductile fracture initiation has taken place in mini-CT specimen at the load level before $J_{0.2\,mm}$. Thus further demonstrates that it is appropriate to consider $J_{0.2\,mm}$ as the critical fracture toughness corresponding to crack initiation. Besides, $J_{0.2\,mm}$ also plays a role in avoiding the effect of the divergence in the analytical expression of blunting line caused by different standards.

It should be noted that, the *J-R* curve that we usually talk about is an exponential fitting of the measured J-Δa points between the 0.15 mm and 1.5 mm exclusion lines, which thus shows a quite large deviation from the original data points in the region outside the exclusion lines (see Figure 2-a). Therefore, in order to compare the real critical J-integral of 1T-CT and mini-CT corresponding to crack initiation, in this study, $J_{0.2\,mm}$ is defined as the intersection of the original J-Δa curve and the 0.2 mm offset line that is parallel to the Y axis (see Figure 2).

Four typical reactor pressure vessel (RPV) steels, 22NiMoCr37, 18MND5, A533B and A106 have been used for this study. The chemical composition is given in Table 1. Present study mainly focuses on the fracture toughness of CT specimens in upper shelf, the mechanical properties of the three steels were generated from tests on mini round tensile bars with 15 mm gauge length and 3 mm diameter at corresponding temperatures. The mechanical properties of the steels at 25 °C and the flow properties used in the subsequent finite element simulations are given in Table 2. Bridgman's stress correction [6] was applied to give an approximation of the true stress at fracture.

Table 1: CHEMICAL COMPOSITIN (WEIGHT%)

Material	C	Si	Mn	S	P	Cr	Ni	Mo	Cu
22NiMoCr37	0.22	0.23	0.88	0.004	0.006	0.39	0.84	0.51	0.08
18MND5	0.18	0.25	1.6	0.002	0.007	0.17	0.64	0.5	0.13
A533B Cl.1	0.183	0.231	1.49	0.0031	0.0073	0.17	0.642	0.479	0.062
A106	0.24	0.23	1.08	0.011	0.011	0.09	0.11	0.04	0.09

Table 2: MECHANICAL PROPERTIES

Material	T (°C)	E (GPa)	ν	σ_y (MPa)	ε_{uts}	σ_{uts} (MPa)	σ_F (MPa)	$\sigma_{F,Bridgman}$ (MPa)
22NiMoCr37*	25	207	0.3	458	0.104	611	1358	1055
18MND5	25	207	0.3	527	0.089	654	1340	1051
18MND5*	290	189.6	0.3	463	0.105	644	1243	992
A533B Cl.1*	25	207	0.3	513	0.088	649	1181	928
A106	25	173	0.3	342	-	568	-	-

*: conditions to be simulated by finite element method (FEM).

T is the test temperature (°C), σ_y is the yield strength (MPa), σ_{uts} is the ultimate tensile strength (MPa), ε_{uts} is the uniform elongation (--), σ_F is the true stress at fracture initiation (MPa), $\sigma_{F\ Bridgman}$ is the corrected true fracture stress for necking (MPa), E is the Young's modulus (MPa) and ν is the Poisson's ratio.

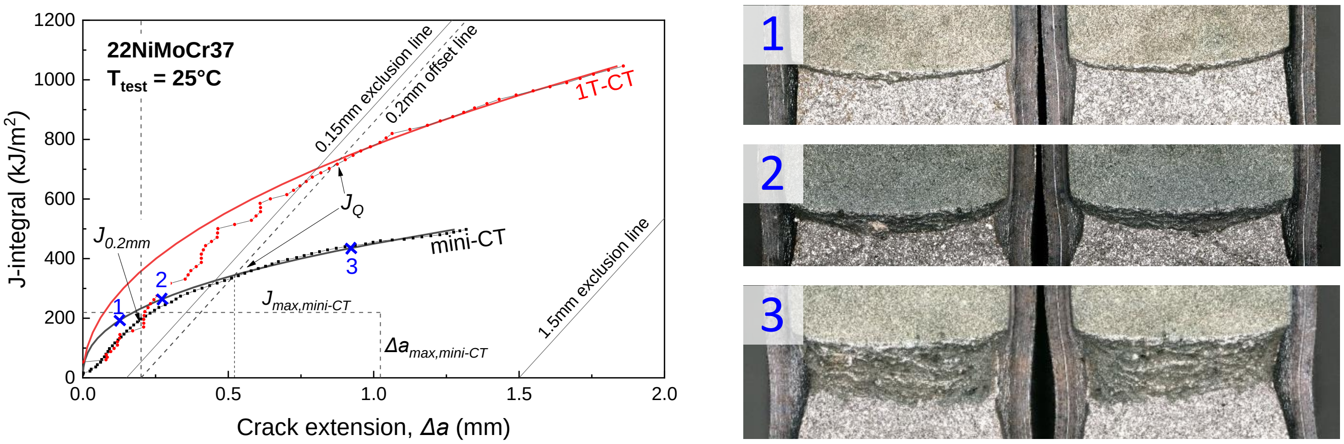

(a)

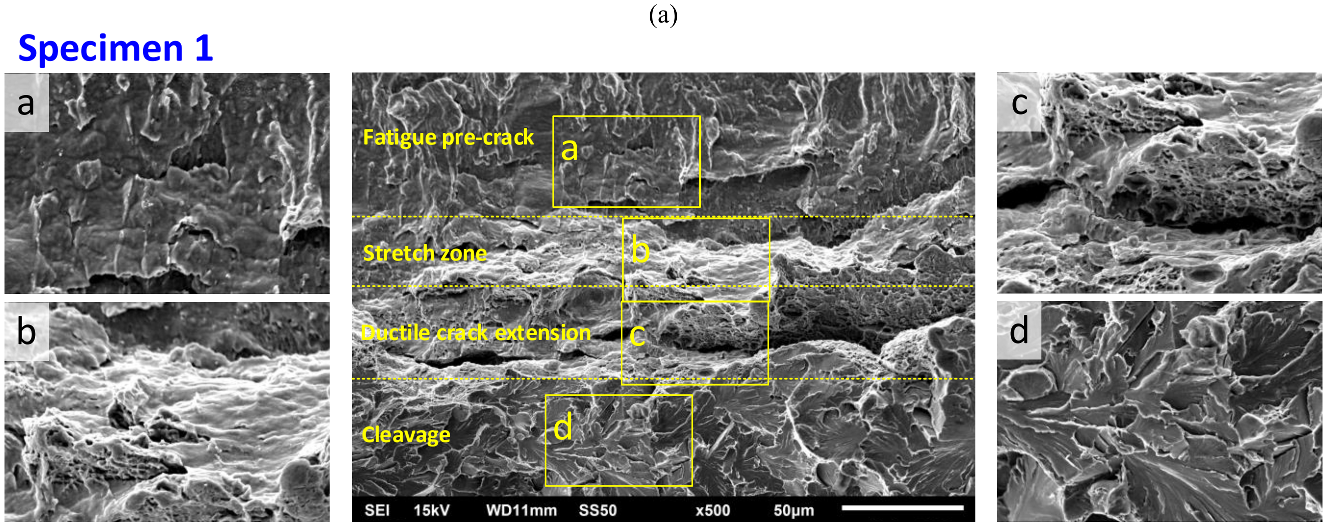

(b)

Figure 2: (a) DETERMINATION OF $J_{0.2\,mm}$ AND J_Q BASED ON THE CRACK RESISTANCE CURVES OF MINI-CT AND 1T-CT, (b) SCANNING ELECTRON MICROSCOPY (SEM) PHOTOS OF THE FRACTURE SURFACE IN SPECIMEN 1

For each material, compact tension specimens with thickness B = 25 mm (1T-CT) and B = 4.15 mm (mini-CT) have been tested at 25 °C (RT) and also at higher temperatures [7]. All specimens were 20% side-grooved and, were tested according to the ASTM E1820 test procedure [4] using a constant test speed of 0.2 mm/min for mini-CT and 1mm/min for 1T-CT. Every test has been analyzed using four different techniques: the unloading compliance technique (UC), the potential drop technique (PD), the normalization data reduction technique (NDR) and the energy normalization technique (EN) [3]. Figure 3 gives an example of how to determine $J_{0.2\,mm}$ from the J-Δa trajectories of the mini-CT specimens tested at the same temperature. For the same specimen, the four techniques lead to the same final J-Δa point corresponding to the final crack extension before final unloading but might differ at $\Delta a = 0.2$ mm. Duplicated tests may also lead to different J-Δa curves which increases the scatter of $J_{0.2\,mm}$. To keep the J-Δa curve variability within a reasonable range of ± 15%, for each material and test temperature, only the curves that are within ± 15% are considered for the calculation of the average $J_{0.2\,mm}$ value. Finally, the selected $J_{0.2\,mm}$ values are presented in Table 3.

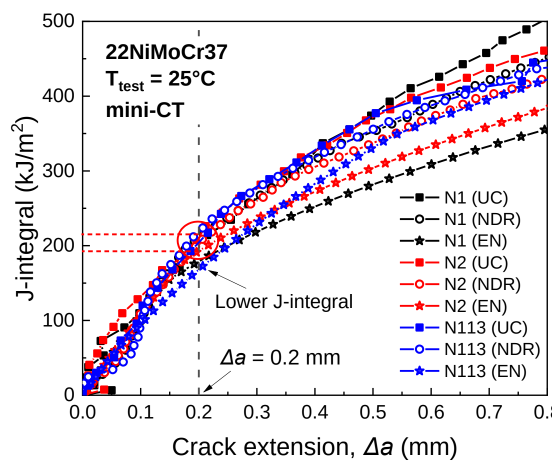

Figure 3: J-Δa TRAJECTORIES OBTAINED FROM MINI-CT SPECIMENS TESTED AT 25 °C USING DIFFERENT TECHNIQUES

Table 3: CRITICAL TOUGHNESS $J_{0.2\ mm}$ MEASURED FROM 1T-CT AND MINI-CT SPECIMENS

Material	T (°C)	Specimen type	Specimen ID	$J_{0.2\ mm}$ (kJ/m^2)			
				UC	PD	NDR	EN
22NiMoCr37	25	mini-CT	N1	202	-	211	179
			N2	211	-	203	193
			N113	204	-	218	(168)*
		1T-CT	N9	(158)	(152)	194	214
			N10	203	(253)	204	214
	150	mini-CT	N3	(149)	-	186	(155)
			N4	191	-	196	(151)
		1T-CT	N11	226	212	(162)	197
			N12	(393)	224	(171)	197
	290	mini-CT	N5	174	(136)	172	(120)
			N6	190	(144)	175	(133)
		1T-CT	N13	225	(151)	178	202
			N14	(371)	(164)	195	202
18MND5	25	mini-CT	M1	223	-	220	194
			M2	235	-	224	204
		1T-CT	M9	226	(294)	234	238
			M10	226	272	250	238
	150	mini-CT	M3	172	(97)	193	(142)
			M4	187	-	193	(139)
		1T-CT	M11	(284)	227	205	220
			M12	(258)	228	203	220
	290	mini-CT	M5	148	(132)	157	(112)
			M6	154	(129)	171	(113)
		1T-CT	M13	(243)	210	198	211
			M14	209	(160)	218	203
A533B Cl.1	25	mini-CT	B1	197	208	193	191
			B2	211	192	197	(157)
		1T-CT	B6	230	219	195	220
			B7	229	227	240	220
	290	mini-CT	B3	161	138	162	(112)
			B4	145	137	158	(101)
		1T-CT	B8	(241)	166	164	173
			B9	(218)	158	163	156
A106	25	mini-CT	A1	132	127	137	(110)
			A2	145	147	148	132
		1T-CT	A1_01-04	(223)	178	(126)	177
			B4_01-03	188	(234)	(121)	176

*: data in brackets are excluded due to large deviations.

The overall results are summarized in Table 4, where average $J_{0.2\ mm}$ values obtained using different techniques under the same conditions (same material and test temperature) are presented. The results show a slightly systematic underestimation of the $J_{0.2\ mm}$ measured with mini-CT specimens with respect to the values obtained from 1T-CT specimens. Considering the ratio of average $J_{0.2\ mm}$ between 1T-CT and mini-CT listed in the last column, we obtain a ratio that is systematically larger than 1. The $J_{0.2\ mm,\ 1T\text{-}CT}/J_{0.2\ mm,\ mini\text{-}CT}$ - ratio values presented in Table 4 are plotted in Figure 4. It is shown that most data points fall between the ratio of 1 and 1.2, with only two data points (18MND5 at 290 °C and A106 at RT) being much larger. The average ratio yields the value of 1.15, which indicates a good correspondence between different specimen geometries when using $J_{0.2\ mm}$ as an initiation fracture toughness. However, to improve the statistical significance of those results, three test conditions with representative ratios: 18MND5 at 290 °C (with the maximum ratio), 22NiMoCr37 at RT (with the minimum ratio) and A533B at RT (with a ratio close to the average) were investigated in the following sections with the help of finite element method (FEM).

Table 4: AVERAGE $J_{0.2\ mm}$ MEASURED FROM 1T-CT AND MINI-CT SPECIMENS

Material	T (°C)	Average $J_{0.2\ mm}$ (kJ/m^2) mini-CT	Average $J_{0.2\ mm}$ (kJ/m^2) 1T-CT	$J_{0.2\ mm,1T\text{-}CT}$ / $J_{0.2\ mm,mini\text{-}CT}$
22NiMoCr37	25	203	206	1.02
	150	191	211	1.11
	290	178	200	1.13
18MND5	25	217	241	1.11
	150	186	217	1.17
	290	158	208	1.32
A533B Cl.1	25	198	223	1.12
	290	150	163	1.09
A106	25	138	180	1.30

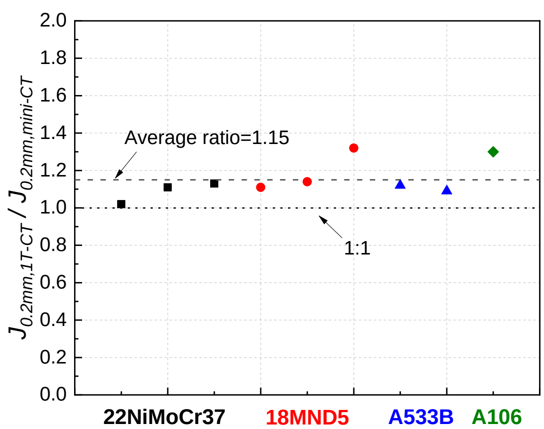

Figure 4: RATIO OF $J_{0.2\ mm}$ MEASURED FROM 1T-CT AND MINI-CT SPECIMENS

3. FINITE ELEMENT PROCEDURES

Non-linear finite element simulations were performed using the commercial package ANSYS. The J_2 flow theory was assumed based on the power law

$$\frac{\sigma}{\sigma_{ys}} = \begin{cases} \frac{E\varepsilon}{\sigma_{ys}} & \text{when } \sigma < \sigma_{ys} \\ \left(1 + \frac{E\varepsilon^{pl}}{\sigma_{ys}}\right)^n & \text{when } \sigma > \sigma_{ys} \end{cases} \tag{1}$$

where n is the strain-hardening exponent.

Figure 5 shows the typical finite element model utilized in the analysis of 20% side grooved mini-CT specimen. Except for the difference in size, the finite element model for the 1T-CT specimen has very similar features. The compact tension specimen was analyzed using one-half of the 3-D model with a symmetric boundary condition imposed on the remaining ligament plane. The CT model was loaded by applying displacement increments to the pin model, which was modeled as a rigid body. Contact elements were applied between the specimen and the pin to simulate the interaction. The meshing was highly refined in the mean crack tip region, a "spider web" [8] mesh configuration with concentric rings of quadrilateral elements was built to provide reliable local J-integral evaluation when necessary. The fatigue pre-crack was modeled as an initial notch with finite notch radius, ρ_0. Prior research have shown that the potential effects of the initial crack-tip notch radius on the stress and strain fields at the near tip region is negligible when the notch radius is small enough. A general suggestion is to keep the initial crack-tip notch radius at least 5 times lower than the CTOD at fracture initiation [9-12]. In addition, subsequent calculations showed that almost identical scaling results are provided by the configurations with ρ_0 = 0.005 mm and ρ_0 = 0.01 mm. Therefore, the effect of notch radius was considered to be limited when $\rho_0 \leq 0.01$ mm, and if any, it can be compensated by sufficient mesh refinement. However, it should be noted that, an extremely small notch radius is also undesirable because it may lead to unexpected extensive element distortion at the near tip region and poor convergence of numerical simulation at higher load levels, such as a notch radius of ρ_0 = 0.0025 mm [12, 13]. Therefore, in the present study, in order to ensure the entire loading history up to the approximate initiation point can be analyzed, and also to ensure the accuracy of the calculation results, the notch radius at the pre-crack tip, ρ_0, was 10 μm (0.01 mm). It can be considered reliable given that it is much smaller than the critical CTOD (0.26 mm).

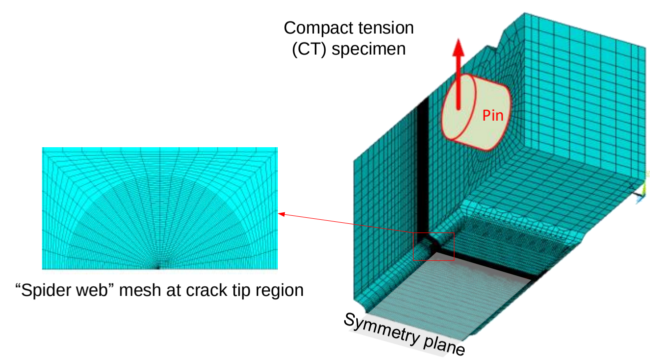

Figure 5: FINITE ELEMENT MODEL OF CT SPECIMEN

4. EFFECT OF LOSS OF CONSTRAINT ON THE INITIATION OF DUCTILE FRACTURE

4.1 Micromechanical-based models of ductile fracture

Prior studies have demonstrated that a micromechanical approach can provide an effective simulation of the void nucleation, void growth and void coalescence of ductile fracture under varying conditions of constraint [14]. In this paper, for the simulation of RPV steels, the void nucleation is neglected, the void growth and void coalescence are assumed to be the dominant mechanisms of the damage process. Two models are applied: the Rice-Tracey void growth model and the Thomason void coalescence model.

Before the void coalescence takes place, ductile fracture is dominated by the void growth. The Rice-Tracey void growth model (R-T model) is used to evaluate the evolution of the void size before the localization occurs. Early studies regarding the growth rate of microvoids [15, 16] have demonstrated that the void growth is mainly dependent on the magnitude of the stress triaxiality and of the equivalent plastic strain:

$$\frac{dR}{R} = \alpha e^{1.5T} d\varepsilon_{eq}^{p} \tag{2}$$

where ε_{eq}^{p} is the equivalent plastic strain; T is the stress triaxiality which is defined as the ratio of hydrostatic stress and Von Mises equivalent stress, $T = \sigma_m/\sigma_{eq}$; dR/R is the growth rate of microvoids; α is the dilatation rate factor which is determined to be 0.427 [17].

As the deformation of the material develops, the void growth process is interrupted by the onset of void coalescence. At this stage, the plastic flow starts to localize inside the ligament between the microvoids, while the material other than the ligament region unloads elastically [14], the initiation of fracture then proceeds. In this paper, the onset of void coalescence is simulated using the Thomason void coalescence model [18, 19]. This model assumes that the onset of the void coalescence occurs when the normalized maximum axial stress, σ_{max}/σ_0, reaches the critical load defined by $I(\chi)$, where σ_0 is the yield stress of the material. It can be expressed as:

$$\frac{\sigma_{max}}{\sigma_0} - I(\chi) \geq 0 \tag{3}$$

Where $I(\chi)$ is the critical damage factor whose value depends on the microstructure of the material:

$$I(\chi) = [1 - \chi^2]\left[\alpha\left(\frac{1-\chi}{\chi}\right)^2 + \beta\chi^{-\frac{1}{2}}\right] \tag{4}$$

where χ is the relative void spacing (void ligament size ratio), $\chi = R_r/L_r$ (see Figure 6). α and β are two constants which depend on the value of strain hardening exponent n, following the research of Pardoen and Hutchinson [10, 20], α and β are defined as $0.1+0.217n+4.83n^2$ and 1.24 respectively, for $0 \leq n \leq 0.3$.

As shown in equation (5), χ is the dominant controlling parameter of the onset of void coalescence, $\chi = R_r/L_r$ can be written as:

$$\chi = \frac{R_r}{L_r} = \frac{R_r}{R_0}\frac{R_0}{L_{r0}}\frac{L_{r0}}{L_r} \tag{5}$$

where subscript "*r*" indicates the direction normal to loading (see Figure 6), subscript "*0*" indicates the initial values. R_r and L_r are the dimensions of the void and the representative volume element in the r direction. $R_0/L_{r0} = \chi_0$ is the relative initial void spacing, which relies on the initial porosity and initial void shape [14]. L_{r0}/L_r is the deformation of the representative volume element in the r direction. Due to the limited voids elongation at crack tip before fracture initiation, $R_r = R_z$ (R_z is the dimension of the void in the direction parallel to loading) is assumed. In this case, R_r can be expressed as the radius of the void after deformation, and R_r/R_0 is the ratio of current void radius and initial void radius, which can be computed using R-T void growth model.

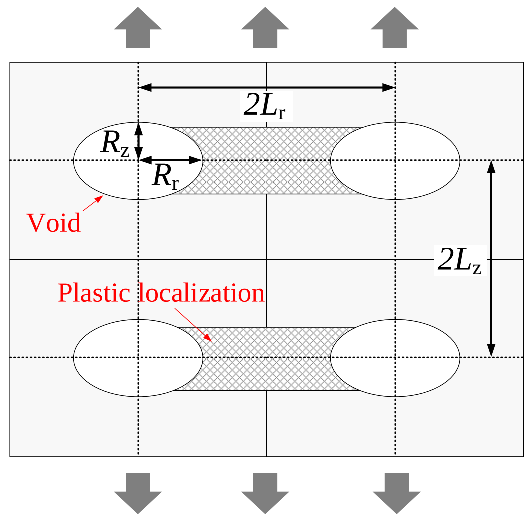

Figure 6: THE DIMENSION PARAMETERS IN THE EQUATION OF I FACTOR

Ductile fracture is assumed to initiate when the onset of void coalescence criterion is satisfied over the characteristic length l^*, the associated expression can be written as:

$$\frac{\sigma_{max}}{\sigma_0} - I(\chi) \geq 0 \quad for \quad r \geq l^* \tag{6}$$

The schematics of this approach is shown in Figure 7, the variations of σ_{max}/σ_0 and $I(\chi)$ in front of the crack tip at various J levels ($J_1 < J_2 < J_3$) are plotted. As the applied load increases, I factor decreases while σ_{max}/σ_0 remains relatively constant. The fracture initiation condition is satisfied over a gradually increasing distance until the latter exceeds the characteristic length l^* and then initiation of ductile fracture occurs.

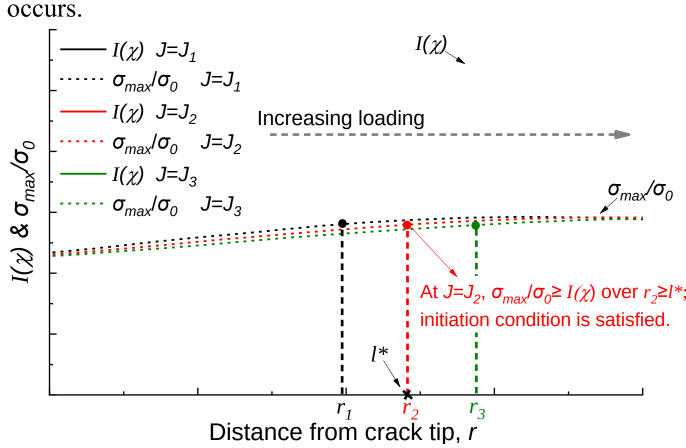

Figure 7: SCHEMATIC OF THE MICROMECHANICAL APPROACH IN CHARACTERIZING FRACTURE INITIATION

It should be noted that, although the micromechanical-based model is simple, the motivation for using this model lies in its ability to take into account the effects of both stress triaxiality and plastic strain on ductile fracture. Instead of providing accurate predictions which are not available and outside the scope of the present work (see e.g. further extensions in references [21, 22]), the micromechanical-based model is used mainly for the aim of providing a simple and fundamental way to quantify the effect of loss of constraint, the effect of test temperature and, later, the irradiation effect.

4.2 Comparison of the critical fracture toughness of 1T-CT and mini-CT

Two inter-dependent parameters in the micromechanical model require identification: the characteristic length l^* and the initial relative void spacing χ_0. Previous studies have developed a framework for determining these two parameters based on experiments and finite element simulations [23]. The initial relative void spacing, χ_0, is calibrated based on the tests on notched round tensile specimens. It is found to be the value that allows the onset of void coalescence criterion to be achieved ($\sigma_{max}/\sigma_0 \geq I(\chi)$) at the center of the narrowest cross section of a notched round tensile specimen at the load corresponding to the experimentally determined crack initiation (sudden drop of applied load). By repeating the same identification procedure on a number of notched round tensile specimens, an approximate range of χ_0 can be obtained, thereby increasing the robustness of the results. Once a χ_0 is fixed, the characteristic length, l^*, is calibrated based on experimentally measured $J_{0.2\ mm}$ and finite element simulations. The J-trial l^* trajectory for a certain material and test temperature is firstly generated by calculating the J-integral where the Thomason criterion is first satisfied (when $\sigma_{max}/\sigma_0 \geq I(\chi)$ for $0 \leq r \leq l^*$) for a given choice of trial length scale. Then based on the J-trial l^* trajectory, the final l^* is determined as the trial characteristic length value that corresponds to the experimental $J_{0.2\ mm}$ value [24], thereby establishing the connection between the macroscopic fracture parameters and the local mechanical properties of the material. Further, the examination on the longitudinal cross section of interrupted notched tensile specimens and the fracture surface of mini-CT specimens can provide an approximate range of l^* from a microstructural perspective.

The average of measured $J_{0.2\ mm}$ displayed in Table 4 exhibits a limited effect of loss of constraint (size effect) on the initiation of ductile fracture. In this section, the micromechanical based approaches as well as finite element simulations are employed to support the experimental observations on the effect of constraint loss and also to provide an accurate quantification of the effect of constraint loss on critical fracture toughness. The test data of 22NiMoCr37 at 25 °C is the first case to be examined because of remarkable lower $J_{0.2\ mm,1T\text{-}CT}/J_{0.2\ mm,mini\text{-}CT}$ ratio (see Figure 4). Figure 8 (a) displays the near tip stress triaxiality and equivalent plastic strain distribution in a mini-CT and 1T-CT at the J-level corresponding to the $J_{0.2\ mm}$ measured at RT of about 200 kJ/m^2. The distance from crack tip, r, is normalized by J/σ_0. A loss of constraint is clearly observed for the mini-CT specimen at the load level close to the crack initiation. Much lower near tip stress triaxiality is observed, but significantly higher equivalent plastic strain is experienced at the same time. However, the combination of those two parameters in the framework of equation (2) compensates for these differences. Figure 8 (b) plots the distribution of $I(\chi)$, which is a damage factor that reveals the progress of ductile fracture. The close agreement between the two curves indicates that mini-CT and 1T-CT have similar level of failure until this load level, further demonstrating the similar critical fracture toughness $J_{0.2\ mm}$.

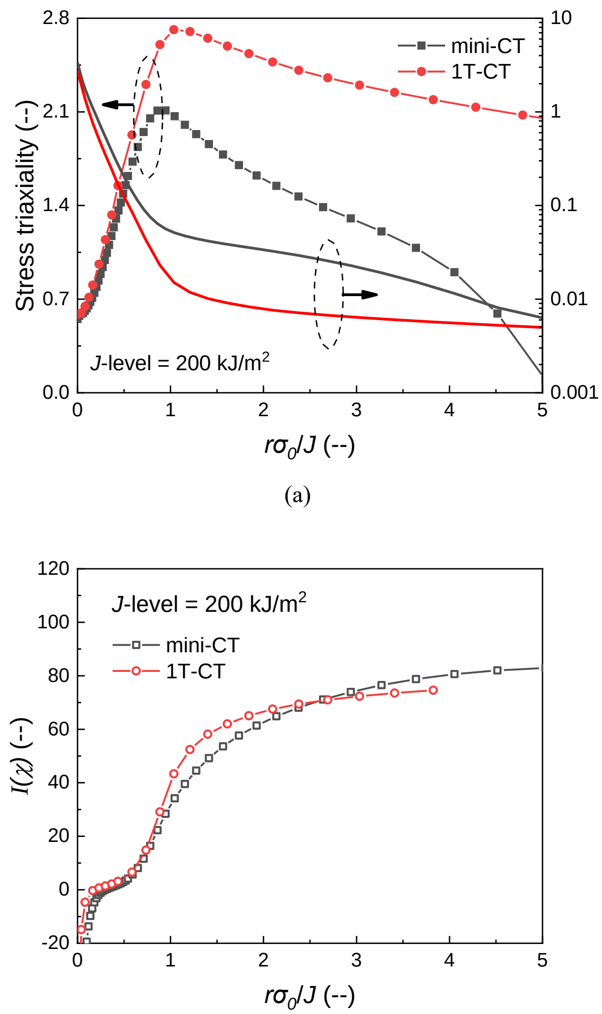

(a)

(b)

Figure 8: DISTRIBUTION OF (a) STRESS TRIAXIALITY AND EQUIVALENT PLASTIC STRAIN AND (b) $I(\chi)$ AT THE MID-THICKNESS POSITION IN FRONT OF THE CRACK TIP OF 1T-CT AND MINI-CT

Then, the critical fracture toughness of mini-CT and 1T-CT are compared. In the analysis to be discussed, the two fitting parameters were fixed to values of $\chi_0 = 0.0456$ and $l^* = 0.23$ mm, respectively, which have been demonstrated to be effective and reasonable in the calculation of $J_{0.2\ mm}$ for

22NiMoCr37 [23]. Figure 9 provides the J-trial l^* trajectories of mini-CT and 1T-CT for 22NiMoCr37 steel at 25 °C, the experimentally measured $J_{0.2\,mm}$ is indicated on the Y axis for reference. The initiation of the ductile fracture is generally observed at the mid-thickness position of CT specimens. So, the high stress zone close to the mid-thickness position provides the most favorable condition to trigger the ductile fracture. Fracture initiation predictions were made at the mid-thickness position, the J-trial l^* curves are all generated based on the local stress and strain at this thickness position. In the plots, the vertical dashed line represents the calibrated l^*, thereby the $J_{0.2\,mm}$ value is determined as the J corresponding to the intersection point of the curves with this dashed line. The $J_{0.2\,mm}$ for the mini-CT then yields the value of 201 kJ/m^2, the $J_{0.2\,mm}$ for the 1T-CT yields the value of 222 kJ/m^2. Recalling the average value listed in Table 4, the calculated $J_{0.2\,mm}$ values for mini-CT and 1T-CT agree well with the measured values, only with an average increase of 7 kJ/m^2. It should be noted that, the ratio of calculated $J_{0.2\,mm}$ of 1T-CT and mini-CT equals to 1.10, which is slightly closer to the average ratio obtained from experimental data. Therefore, it can be stated that the measured low $J_{0.2\,mm}$ ratio is influenced by the statistical nature of the experimental data to a certain extent.

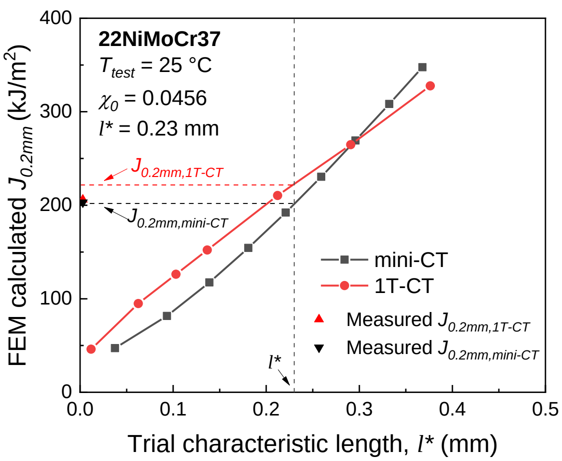

Figure 9: DETERMINATION OF $J_{0.2\,mm}$ FOR 1T-CT AND MINI-CT SPECIMENS ON 22NIMOCR37 AT 150°C

Additional investigations of the effect of constraint loss on the initiation of ductile fracture are performed based on the test data of 18MND5 at 150 °C and A533B at 290 °C. In the context of lacking the tests of notched round tensile specimens, the initial relative void spacing, χ_0, can be equivalently derived from the initial void volume fraction, f_0. Assuming that the void shape is a spheroid, then χ_0 is given by:

$$\chi_0 = \left(\frac{6}{\pi} f_0\right)^{\frac{1}{3}} \tag{7}$$

FRANKLIN's formulae provides an estimation of f_0 for the steel that contains the non-metallic MnS inclusions [25]:

$$f_0 = 0.054\left(S\% - \frac{0.001}{Mn\%}\right) \tag{8}$$

where S and Mn are the proportional content of sulphur and manganese in the material. Based on this equation, the χ_0 yields the value of 0.052 for 18MND5 and 0.063 for A533B. It should be noted that, χ_0 yields the value of 0.066 for 22NiMoCr37 when using FRANKLIN's formulae, which is larger than the value used above. In the present application, χ_0 and l^* are interdependent parameters, which means that, the potential effect of the variation of χ_0 will be compensated by the value of l^*. Further calculations show that the calculated ratio yields the value of 1.06 when $\chi_0 = 0.066$ is adopted for 22NiMoCr37, which is remarkably close to the ratio obtained above. Therefore, χ_0 should be interpreted as a parameter that reflects the relative properties of different materials, rather than an accurate descriptor of the microscopic feature.

Figure 10 (a) and (b) provide the J-trial l^* trajectories of mini-CT and 1T-CT for 18MND5 steel at 290°C and A533B steel at 25 °C, respectively, the experimentally measured $J_{0.2\,mm}$ values are indicated on the Y axis for reference. The l^* values for these two materials are determined using the measured $J_{0.2\,mm}$ of mini-CT, based on which, the $J_{0.2\,mm}$ of 1T-CT can be determined as the J corresponding to this l^*, thereby establishing the scaling of $J_{0.2\,mm}$ between 1T-CT and mini-CT. For the 18MND5 steel, l^* is determined to be 0.19 mm based on the measured $J_{0.2\,mm}$ of mini-CT, the $J_{0.2\,mm}$ of 1T-CT then yields the value of 184 kJ/m^2. The ratio between the calculated $J_{0.2\,mm}$ of 1T-CT and the $J_{0.2\,mm}$ of min-CT equals to 1.16, which is remarkably closer to the average value than the measured ratio (1.32). Therefore, the high ratio exhibited by 18MND5 at 290 °C due to statistical effects is corrected to a reasonable range. For the A533B steel, following the same procedure, the $J_{0.2\,mm}$ of 1T-CT is determined to be 231 kJ/m^2. The ratio between the calculated $J_{0.2\,mm}$ of 1T-CT and the $J_{0.2\,mm}$ of mini-CT is around 1.17, still quite close to the ratio of 1.12 which is observed from the experimental data. Previous research based on the test data and the microstructure of notched round tensile specimens provided an approximate reasonable range of χ_0 and l^* for 22NiMoCr37 [23]. That is, the 95% confidential bound of χ_0 ranges from 0.032 to 0.064, and l^* ranges from 0.075 mm to 0.273 mm. As two other typical RPV steels with similar properties, the χ_0 and l^* of 18MND5 and A533B are in the same order of magnitude, which is reasonable. Although the determination of χ_0 and l^* plays a crucial role in the scaling of initial fracture toughness between 1T-CT and mini-CT, it can be seen from the J-trail l^* trajectories of 18MND5 and A533B that when l^* varies (due to different identification methods) within a reasonable range, the relative value of $J_{0.2\,mm,1T\text{-}CT}$ and $J_{0.2\,mm,mini\text{-}CT}$ will still be only slightly different and will not affect the current conclusion.

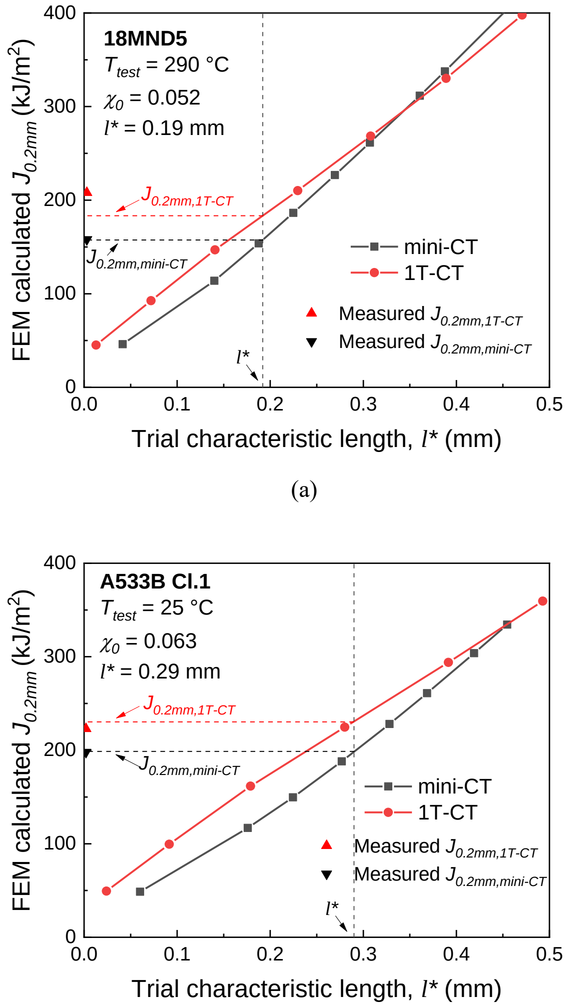

(a)

(b)

Figure 10: DETERMINATION OF $J_{0.2\ mm}$ FOR 1T-CT AND MINI-CT SPECIMENS ON (1) 18MND5 AT 150°C AND (2) A533B AT 290°C

To summarize, finite element simulations and micromechanical based approaches are combined to study three typical test cases:

(1) 22NiMoCr37 material at 25 °C with the lowest $J_{0.2\ mm}$ ratio of around 1.02,

(2) 18MND5 material at 290 °C with the highest $J_{0.2\ mm}$ ratio of around 1.32, and

(3) A533B material at 25 °C with a ratio close to the average.

The calculated $J_{0.2\ mm,1T\text{-}CT}/J_{0.2\ mm,mini\text{-}CT}$ - ratio values for these three cases are 1.10, 1.16 and 1.17, respectively. As shown in Figure 11, when the original measured ratio is corrected to the calculated ratio, ignoring the scatter caused by the experimental uncertainty, a general feature that the $J_{0.2\ mm}$ for 1T-CT is only slightly larger than that for mini-CT can be observed. Therefore, the effect of loss of constraint on the initiation of ductile fracture can be considered as limited. The following simple size correction for the critical fracture toughness ($J_{0.2\ mm}$) which relies on the experimental observations and FEM simulations can be applied when necessary, i.e. $J_{0.2\ mm,1TCT} = 1.15 * J_{0.2\ mm,mini\text{-}CT}$.

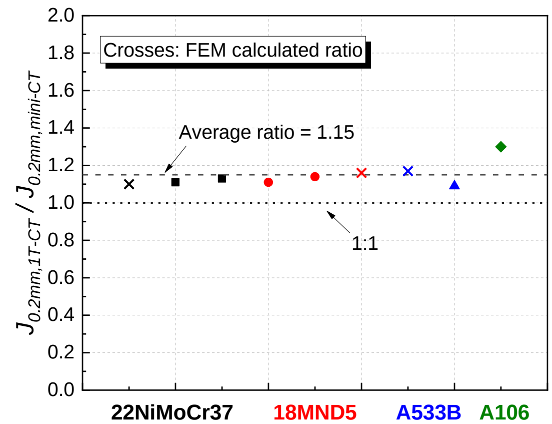

Figure 11: CORRECTED RATIO OF $J_{0.2\ mm}$ MEASURED FROM 1T-CT AND MINI-CT SPECIMENS

CONCLUSION

This work investigates the potential effect of constraint loss on the initiation of ductile fracture in a mini-CT, where subsequent crack resistance curve is significantly underestimated. Micromechanical based approaches and finite element simulations are combined to provide accurate assessment on the scaling of critical fracture toughness for 1T-CT and mini-CT geometries. The results show that the effect of constraint loss on the initiation of ductile fracture is limited, and a size scale parameter of 1.15 can be applied to the critical fracture toughness ($J_{0.2\ mm}$) of mini-CT specimen to estimate the value that would have been obtained from 1T-CT specimen.

ACKNOWLEDGEMENTS

The present work was performed within the SUSTAIN project at SCK CEN supported by the NMS management. In addition, part of the work was done under the FRACTESUS project that has received funding from the Euratom research and training program 2020-2024 under grant agreement No. 900014. The authors gratefully acknowledge the support of the technical staff of LHMA at SCK CEN. The authors also acknowledge SCK CEN Academy for PhD funding. Additionally, the authors would like to acknowledge the late Dr. Tomasz Brynk for his extensive contributions to this work.

REFERENCES

[1] M. Li, R. Chaouadi, I. Uytdenhouwen, and T. Pardoen, *Size correction scheme to determine fracture toughness with mini-CT geometry in the transition regime.* Submitted, 2023.

[2] ASTM, *ASTM E1921-19b*, in *Standard Test Method for Determination of Reference Temperature, T_0, for Ferritic Steels in the Transition Range*. 2020, ASTM International: West Conshohocken, PA.
[3] R. Chaouadi, M. Lambrecht, and R. Gérard. *Crack Resistance Curve Measurement With Miniaturized CT Specimen*. in *ASME 2018 Pressure Vessels and Piping Conference*. 2018. American Society of Mechanical Engineers, PVP2018-84690.
[4] ASTM, *ASTM E1820-20b*, in *Standard Test Method for Measurement of Fracture Toughness*. 2020, ASTM International: West Conshohocken, PA.
[5] E. ESIS, *P2-92.* ESIS Procedure for determining the fracture resistance of ductile materials, European Structural Integrity Society (ESIS), 1992.
[6] P. Bridgman, *The stress distribution at the neck of a tension specimen.* Trans. ASM, 1944. **32**: p. 553-574.
[7] E. Lucon, Scibetta, M., Chaouadi, *Use of Miniaturized Compact Tension Specimens for Fracture Toughness Measurements in the Upper Shelf Regime*, in *SCK•CEN Reports*. 2005, SCK CEN: Mol, Belgium.
[8] T.L. Anderson, *Fracture mechanics: fundamentals and applications*. 2017: CRC press.
[9] X. Gao, C. Ruggieri, and R. Dodds, *Calibration of Weibull stress parameters using fracture toughness data.* International Journal of Fracture, 1998. **92**(2): p. 175-200.
[10] T. Pardoen and J. Hutchinson, *An extended model for void growth and coalescence.* Journal of the Mechanics and Physics of Solids, 2000. **48**(12): p. 2467-2512.
[11] C. Ruggieri and R.H. Dodds Jr, *An engineering methodology for constraint corrections of elastic–plastic fracture toughness–Part I: A review on probabilistic models and exploration of plastic strain effects.* Engineering Fracture Mechanics, 2015. **134**: p. 368-390.
[12] C. Ruggieri, R.G. Savioli, and R.H. Dodds Jr, *An engineering methodology for constraint corrections of elastic–plastic fracture toughness–Part II: Effects of specimen geometry and plastic strain on cleavage fracture predictions.* Engineering Fracture Mechanics, 2015. **146**: p. 185-209.
[13] J.P. Petti and R.H. Dodds Jr, *Calibration of the Weibull stress scale parameter, σu, using the Master Curve.* Engineering Fracture Mechanics, 2005. **72**(1): p. 91-120.
[14] A. Pineau, A.A. Benzerga, and T. Pardoen, *Failure of metals I: Brittle and ductile fracture.* Acta Materialia, 2016. **107**: p. 424-483.
[15] J.R. Rice and D.M. Tracey, *On the ductile enlargement of voids in triaxial stress fields∗.* Journal of the Mechanics and Physics of Solids, 1969. **17**(3): p. 201-217.
[16] F.A. McClintock, *A criterion for ductile fracture by the growth of holes.* 1968.
[17] Y. Huang, *Accurate Dilatation Rates for Spherical Voids in Triaxial Stress Fields.* Journal of Applied Mechanics, 1991. **58**(4): p. 1084-1086.
[18] P. Thomason, *A three-dimensional model for ductile fracture by the growth and coalescence of microvoids.* Acta Metallurgica, 1985. **33**(6): p. 1087-1095.
[19] P. Thomason, *Three-dimensional models for the plastic limit-loads at incipient failure of the intervoid matrix in ductile porous solids.* Acta Metallurgica, 1985. **33**(6): p. 1079-1085.
[20] T. Pardoen, M. Scibetta, R. Chaouadi, and F. Delannay, *Analysis of the geometry dependence of fracture toughness at cracking initiation by comparison of circumferentially cracked round bars and SENB tests on Copper.* International journal of fracture, 2000. **103**(3): p. 205-225.
[21] V.-D. Nguyen, T. Pardoen, and L. Noels, *A nonlocal approach of ductile failure incorporating void growth, internal necking, and shear dominated coalescence mechanisms.* Journal of the Mechanics and Physics of Solids, 2020. **137**: p. 103891.
[22] T. Pardoen, F. Scheyvaerts, A. Simar, C. Tekoğlu, and P.R. Onck, *Multiscale modeling of ductile failure in metallic alloys.* Comptes Rendus Physique, 2010. **11**(3-4): p. 326-345.
[23] M. Li, R. Chaouadi, L. Noels, I. Uytdenhouwen, M. Lambrecht, and T. Pardoen, *Investigations on the effect of pre-crack non-uniformity for the mini-CT geometry during ductile fracture.* Submitted, 2023.
[24] T.L. Panontin and S.D. Sheppard, *The relationship between constraint and ductile fracture initiation as defined by micromechanical analyses*, in *Fracture Mechanics: 26th Volume*. 1995, ASTM International.
[25] A. Franklin, *Comparison between a quantitative microscope and chemical methods for assessment of non-metallic inclusions.* J Iron Steel Inst, 1969. **207**(2): p. 181-186.